Progress In Electromagnetics Research, Vol. 145, 273–286, 2014

An Improved Quality Guided Phase Unwrapping Method and Its Applications to MRI

Yudong Zhang[1, 2, *], Shuihua Wang[1, 3], Genlin Ji[1], and Zhengchao Dong[2]

Abstract—An improved method of quality guided phase unwrapping (QGPU) is proposed in this work. It extracts the quality map via a median filtered phase derivative variance (MFPDV) that applies a two-dimensional median filter on the phase derivative variance (PDV) map, in order to reduce the effect of noise in the background area. In addition, we employed the Indexed Interwoven Linked List (I2L2) structure to store the orderly adjoin list more efficiently and the Two Section Guided Strategy (TSGS) to reduce comparison frequency. The experiments demonstrate that the normalized L_1 norm of MFPDV of a brain MR image is only 0.0827, less than that of PDV method at 0.0923. Besides, the computation time of QGPU with I2L2 technique is only 30% of that with sequence structure, and the computation time of QGPU with TSGS is only 65% of that without TSGS. In total, the proposed MFPDV upwrap phase images better than conventional PDV map, and I2L2 and TSGS are efficient strategies to reduce computation time.

1. INTRODUCTION

Many imaging systems, such as magnetic resonance imaging (MRI) [1], synthetic aperture radar [2], optical Doppler tomography [3], fringe projection profilometry [4], acoustic imaging, interferometry [5], and X-ray crystallography, make use of phase information to produce desired images. In the field of MRI, phase information is also very useful in various applications such as magnetic field mapping, noise reduction, and correction of spatial distortion, although the final images are conventionally presented in the magnitude modes [6]. In these imaging modalities and applications, the initial phases of the measured data are obtained by a simple operation of arctangent from the raw complex images and are wrapped in the principal interval $(-\pi, \pi]$. Therefore, the wrapped phases distribute within the limits of $-\pi$ and $+\pi$, and phase discontinuities occur at the limits every time when the unknown true phase changes by 2π. The applications of the phase images require to unwrap the phases in order to remove the discontinuities and to obtain an estimate of the true phases [7].

In the past decades, many new phase unwrapping algorithms have been proposed. In terms of the working domains, these algorithms can be classified into two groups: temporal phase unwrapping and spatial phase unwrapping. The temporal methods are usually effective and robust, but require multi-frames of wrapped phase along the time dimension [8]. The spatial methods of phase unwrapping have fewer restrictions, but it is a challenge to cope with the disjoint regions and phase discontinuities [9]. One of the most promising methods for phase unwrapping in the spatial domain is the quality guided phase unwrapping (QGPU) algorithm, which gains attentions among researchers in recent years. The primary assumption of QGPU is that a good quality map will guide a reasonable unwrapping path and, thereby, reduce the chance of misregistration of phases at the points of phase discontinuities [10].

Received 10 February 2014, Accepted 25 March 2014, Scheduled 2 April 2014

* Corresponding author: Yudong Zhang (zhangyudongnuaa@gmail.com).

[1] School of Computer Science and Technology, Nanjing Normal University, Nanjing, Jiangsu 210023, China. [2] Translational Imaging Division & MRI Unit, Columbia University and New York State Psychiatric Institute, New York, NY 10032, USA. [3] School of Electronic Science and Engineering, Nanjing University, Nanjing, Jiangsu 210046, China.

The QGPU uses quality map to form an adjoin list, and unwraps the phase image pixel by pixel in the order of the adjoin list, and then updates the adjoin list by ordering quality values. Several approaches to calculating quality map have been proposed, which includes phase derivative variance (PDV), correlation map [11], the pseudo-correlation, the maximum phase gradient, first phase difference map, second phase difference map, amplitude map, and Phase Derivative Variance Map [12]. Those methods can extract satisfying quality map but they are vulnerable for noises.

In this paper, we tried to use the median filtered phase derivative variance (MFPDV) to alleviate the eventuality of the noises. The experiments demonstrate its effectiveness. Besides, we introduce in two improvements to reduce computation time, viz., Indexed Interwoven Linked List (I2L2) and Two Section Guided Strategy (TSGS) strategies. The I2L2 can store the adjoin list more efficiently, while the TSGS can reduce the comparison frequency.

The structure of the paper is organized as follows: methodology in next Section 2 describes the simple concept of phase unwrapping, introduces in the QGPU method, and proposes an improved phase unwrapping method. Section 3 contains the experiments and discussions on simulation and realistic data. Section 4 applies the proposed method to MRI and achieves positive results. Final Section 5 is devoted to conclusions and future research.

2. METHODOLOGY

2.1. Phase Unwrapping

The initial phase map obtained by a simple operation of arctangent can only take values in the principal interval $(-\pi, \pi]$. When the measured phase falls outside the interval, integer multiples of 2π are added or subtracted to the measured phase until it is wrapped within the principal interval [13]. The process of phase unwrapping is to recover the true phase from the wrapped phase. The relationship between the unwrapped phase and the wrapped phase is formulated as

$$u(r) = w(r) + 2\pi \times n(r) \tag{1}$$

Here r denotes a selected point in the image; u and w represent the unwrapped & wrapped phase, respectively; n is an integer required to unwrap the phase.

We employ a simple model to illustrate the basic principles of spatial phase unwrapping [14]. Suppose pixel "a" is unwrapped, then its neighbor "b" can be unwrapped as

$$u(b) = w(b) + 2\pi \times \text{round}\left(\frac{u(a) - w(b)}{2\pi}\right) \ s.t. \ -\pi < u(a) - u(b) \leq \pi \tag{2}$$

Here, $u(a)$ and $u(b)$ denote the unwrapped phases of pixel a and b, respectively; $w(a)$ and $w(b)$ denote the wrapped phases of pixel a and b, respectively. After all pixels marked "b" are unwrapped, we can unwrap their neighbor pixels "c", and finally "d", as shown in Figure 1.

In practical situations, however, the spatial unwrapping may fail due to following five potential problems: (i) undersampling causes sharp phase difference exceeding the principal interval; (ii) noise supplies wrong values; (iii) invalid area interferes with the procedures; (iv) real discontinuities are misrecognized as continuities; (v) errors propagate to adjacent pixels and all the following subsequent pixels. Therefore, QGPU is introduced to solve these problems.

2.2. Quality Guided Phase Unwrapping

QGPU can mitigate aforementioned problems. We obtain quality map directly from the raw measurement data, and its value indicates the quality of related pixel. Noisy pixels and invalid areas are labelled low-quality.

Conventional phase unwrapping methods unwrap pixels in the same color (Figure 1) simultaneously based on their unwrapped neighbor pixels [15]. QGPU established a queue called "adjoin list [16]" that is ordered so pixels with low quality are moved backwards while pixels with high quality are moved forwards. Only the pixel with the highest quality is chosen for unwrapping. The pseudocodes of the whole procedure of QGPU (Figure 2) are listed as follows:

Step 1 Generate the quality map from the raw data;

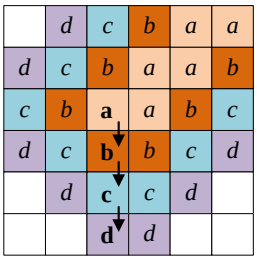

Figure 1. The spatial unwrapping procedure.

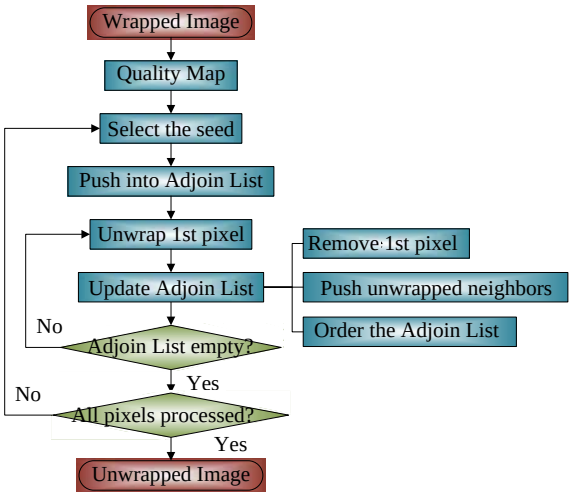

Figure 2. Procedure of QGPU.

Step 2 Select the pixel with the highest quality as the seed; and push it into the orderly adjoin list;

Step 3 Unwrap the first pixel in orderly adjoin list;

Step 4 Update the orderly adjoin list:

Step 4.1 Remove the first pixel from the adjoin list;
Step 4.2 Push its wrapped neighbor pixels into the adjoin list;
Step 4.3 Order the adjoin list according to the quality values.

Step 5 Jump to Step 3 until the adjoin list is empty.

Step 6 Jump to Step 2 until all pixels are processed.

2.3. Median-Filtered PDV

PDV is a commonly used quality map [17]. The pixel is considered the highest quality if its PDV value is the least, and vice versa. However, PDV map is usually noisy, especially in the low SNR regions, where the pixels are severely corrupted by noise. We therefore proposed a Median-Filtered PDV (MFPDV) approach that applied a two-dimensional median filter on the PDV map generated from the phase map. The MFPDV can reduce the noise while reserving the edge and texture structure of the brain. In this study, the size of median filter is 7-by-7.

An example is given in Figure 3. The PDV map found a wrong highest quality pixel at the upper-left corner outsides of the brain (red frames in Figure 3(b)) due to noise. By aid of the median filtering, we suppressed the background noises and obtained a more robust and reliable quality map (Figure 3(c))

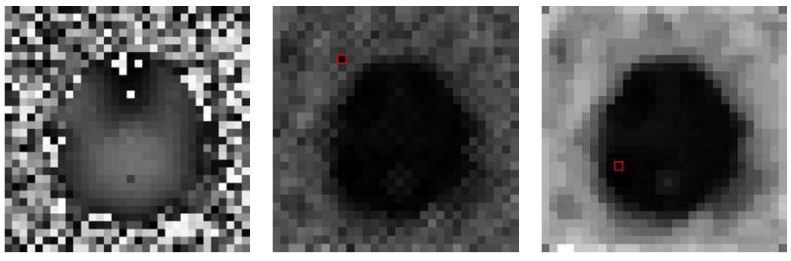

Figure 3. An MRI brain image where dark denotes high quality and white denotes low quality. Pixel with the least value (the highest quality) is marked with red frames. (a) Phase map. (b) PDV map. (c) MFPDV map.

where we obtained the correct highest quality pixel at the bottom-left corner within the brain. We note that the rough structure of the brain is almost maintained and the contrast of the image is enhanced with the help of median filtering.

2.4. Orderly Adjoin List — I2L2

Revisiting Figure 2, adjoin list plays an important role in phase unwrapping. It can be arranged either orderly or disorderly [18]. For an orderly adjoin list, the update procedures consist of three steps: (i) remove the unwrapped pixel; (ii) locate the position for the new pixels; (iii) insert new pixels. For a disorderly adjoin list, there are also three steps: (i) remove the unwrapped pixel; (ii) insert new pixels at the end of the queue; (iii) search the pixel with the highest quality value to unwrap. Figure 4 gives a simple demonstration.

Since the orderly list only needs to visit a part of the adjoin list, while the disorderly list needs to traverse the whole length to find the highest value, we used the orderly adjoin list in this study. The orderly adjoin list can be performed by following four data structures [19]:

- Sequence. The 1D array stores the continuous orderly adjoin list, but it is inefficient to insert or remove pixels owing to memory reallocation.
- Linked List (LL). LL consists of a group of nodes which together represent a sequence. Each node is composed of a datum and a link to the next node in the sequence. This structure allows for efficient insertion or removal of elements from any position in the sequence, but it is time consuming to traverse the whole LL chain due to its very long length.
- Indexed LL (ILL). The ILL cuts the LL into several sections, and each section contains a portion of the whole LL. This structure can be viewed as a 2D array with dynamic horizontal linked list. The quality values in ILL decrease from top to bottom and from left to right. The ILL solves the traversal problem, but the size of each section cannot be predetermined.
- Indexed Interwoven Linked List (I2L2). I2L2 interweave the sections of ILL in pre-allocated sequence. Links distinguish different sections without ambiguity. The index of the 1D sequence of I2L2 is easy to be converted to the 2D subordination of the pixel in the image.

Figure 5 shows the four data structures of orderly adjoin list. Among them, I2L2 is the most successful data structure and it can solve all the problems that the other three data structures cannot. Besides, I2L2 cost nearly the same memory as others with a small amount of extra memory to store the interwoven indexes.

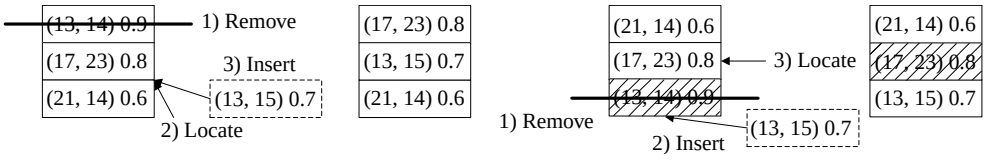

Figure 4. Adjoin list vs. disorderly adjoin list. (a) Orderly adjoin list. (b) Disorderly adjoin list

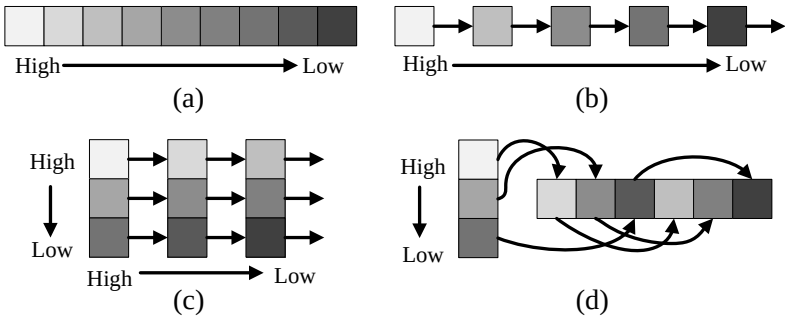

Figure 5. Four data structures of orderly adjoin list. (a) Sequence. (b) LL. (c) ILL. (d) I2L2.

2.5. Two-Section Guided Strategy

In classical QGPU methods, each pixel's quality value is compared with others before unwrapped. However, pixels with high quality usually give correct results even without quality comparison. Based on this, Zhao [9] proposed the TSGS method, which focuses on using a threshold (T) to divide all pixels as high-quality groups and low-quality groups.

$$T = \frac{\text{High-quality Pixels}}{\text{All Pixels}} \tag{3}$$

For high-quality pixels, the comparison can be waived; for low-quality pixels, the comparison still needs to be performed. The threshold T is chosen according to the percentage of the high quality group.

In general, the improvements of our proposed methods fall in three points. 1) We proposed the MFPDV quality map; 2) we used I2L2 structure to store the adjoin list; and 3) we introduced in TSGS to waive partial comparison operations. In total, the proposed method can be depicted as follows.

Step 1 Generate the MFPDV from the raw data;

Step 2 Calculate the threshold so it covers 60% of all pixels (See Section 3.4 as how to obtain the optimal threshold value);

Step 3 Create a adjoin list based on I2L2 structure;

Step 4 Select the pixel with the highest quality as the seed; and push seed into the adjoin list;

Step 5 Unwrap all pixels greater than the threshold in adjoin list;

Step 6 Remove the unwrapped pixel from the adjoin list;
Step 7 Push their wrapped neighbor pixels into the adjoin list;

Step 8 Jump to Step 5 until all pixels in the adjoin list are less than the threshold;

Step 9 Order the whole adjoin list in terms of the quality values, unwrap the 1st pixel in the list;

Step 10 Jump to Step 6 until the adjoin list is empty;

Step 11 Jump to Step 4 until all pixels are processed.

3. EXPERIMENTS

All the programs were developed in-house on the platform Matlab2013a, and run on a HP laptop with Intel Core i3 processor of 3G Hz clock rate, and 2 GB RAM. The readers can repeat the experiments on any computer that install Matlab.

3.1. PDV versus MFPDV

The first experiment is to demonstrate the effectiveness of MFPDV. We evaluate the unwrapped phase by the total amount of phase discontinuity of the unwrapped phase images by the most widely used normalized L_1 norm (NLN) [20] that is defined as

$$\text{NLN} = \frac{\omega_x \left\|\nabla^x g - \nabla^x u\right\|_1 + \omega_y \left\|\nabla^y g - \nabla^y u\right\|_1}{W * H} \tag{4}$$

Here $||\cdot||_1$ denotes the L_1 norm. u and g represent the unwrapped and ground-truth phase image, respectively. ∇^x and ∇^y represent gradients along x-axis and y-axis, respectively. ω_x and ω_y represent the weighted coefficients along x- and y-axis, respectively. Both of them are set as 0.5. W and H represent the width and height of the phase image, respectively.

The normalized L_1 norms of PDV and MFPDV are 0.0923 and 0.0827, respectively. The improvement is significant. Therefore, the proposed MFPDV obtains less phase discontinuity than PDV does. Figure 6 shows that both approaches are able to unwrap the phase in brain area correctly. However, the PDV approach results in larger oscillation than MFPDV in the area outsides the brain. This may potentially inflict a challenge for following procedures such as the reconstruction of image in susceptible weighted imaging.

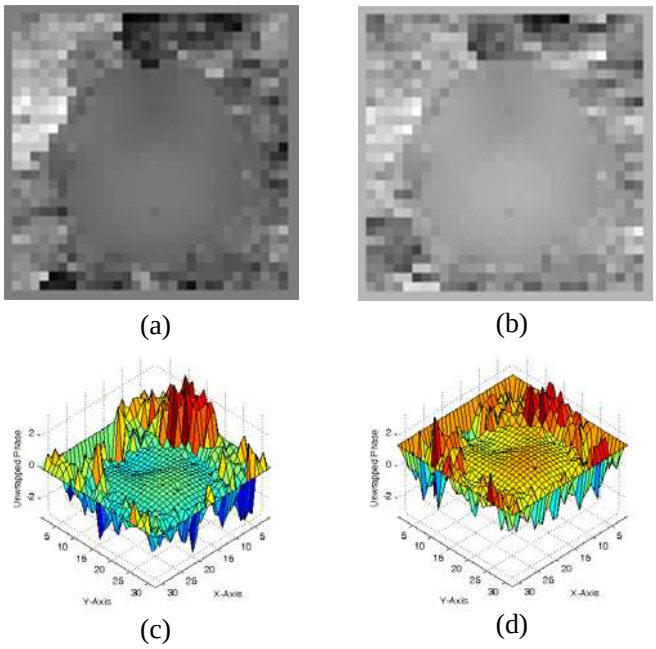

Figure 6. The brain MRI unwrapping phase images (red denotes the highest value and blue the lowest). (a) Recovery by PDV, NLN = 0.0923. (b) Recovery by MFPDV, NLN = 0.0827. (c) 3D rendering of (a). (d) 3D rendering of (b).

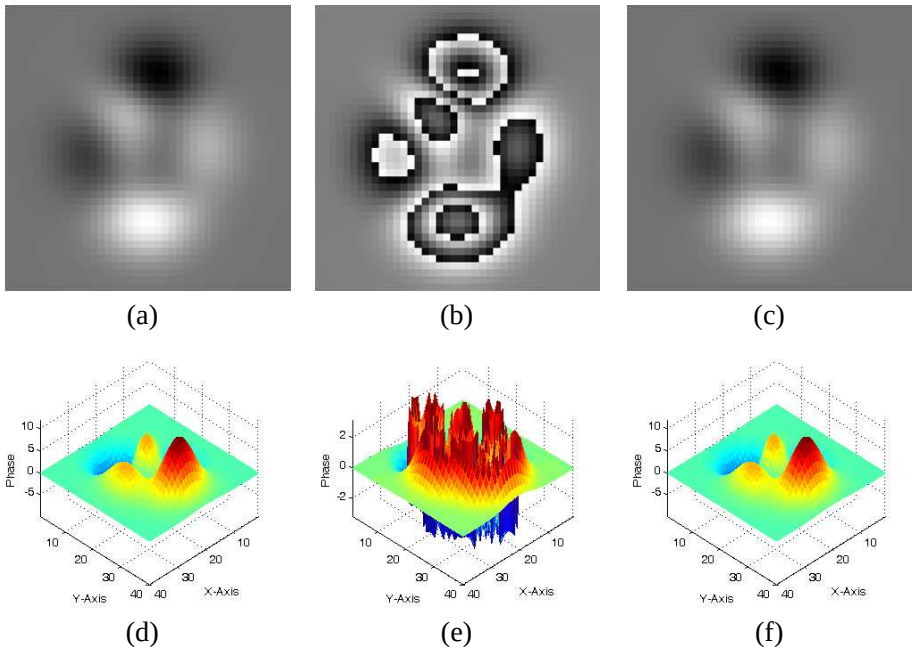

Figure 7. The "peaks" phase image unwrapping. (a) Original phase. (b) Wrapped phase. (c) Unwrapped phase. (d) 3D rendering of (a). (e) 3D rendering of (b). (f) 3D rendering of (c).

3.2. I2L2 versus Other Structures

In the second experiment, we use a simulated 40×40 "peaks" phase image to test the performance of the I2L2 structure. The phase images are obtained by the "peaks" command from Matlab, and are magnified by a factor of 1.5. Figure 7 shows the phase unwrapping results. The I2L2 method achieves

nearly perfect unwrapping, and even the phase values of the background area are the same as those in the original image (Figure 7(a)).

Afterwards, we resize the phase image to different sizes from 10 to 100 with increment of 10. We unwrap every image by I2L2 structure (our method) and other structures (sequence, LL, and ILL). Figure 8 illustrates the time curves versus width of phase image. We notice that the I2L2 runs the fastest among all structures, the second fastest is ILL, followed by LL and sequence. The ranking of the structure in terms of computation speed is coherent to the aforementioned analysis. In average, the I2L2 only cost about 30% time of the sequence structure.

3.3. With TSGS versus without TSGS

In the final experiment, we use another simulated 41×41 "logo" phase image obtained by the "logo" command in Matlab and magnified by 10. Figure 9 shows the phase unwrapping results of the logo phase image.

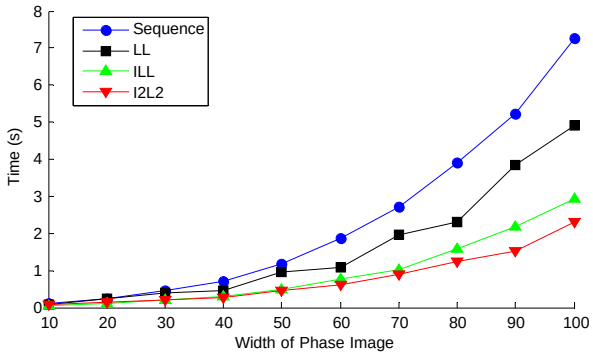

Figure 8. Time Comparison among four structures: sequence, LL, ILL, and I2L2.

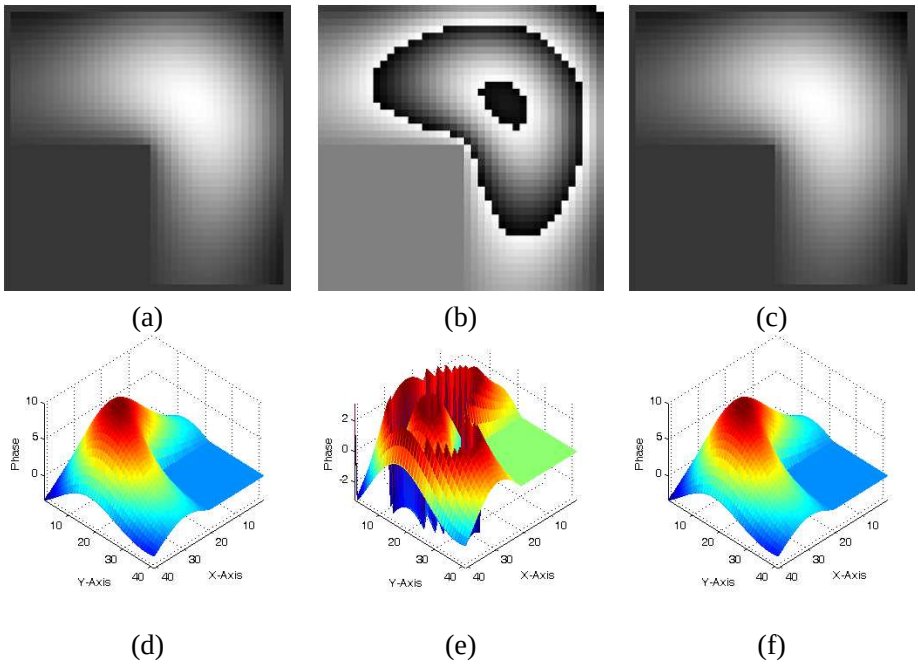

Figure 9. The "logo" phase image unwrapping. (a) Original phase. (b) Wrapped phase. (c) Unwrapped phase. (d) 3D rendering of (a). (e) 3D rendering of (b). (f) 3D rendering of (c).

Similar to experiment in Section 3.2, we resize the "logo" phase image to different sizes from 10 to 100 with increment of 10. We unwrap every phase image with TSGS (our method) and without TSGS. The results in Figure 10 shows the TSGS cost only 65% time compared to the method without TSGS averagely.

3.4. Threshold Choosing

In the final experiment, we change threshold T from 10% to 100% with an increment of 10% to find the optimal threshold. We assess both the calculation times and error rates to select the optimal threshold. Figure 11 draws the curves of time and error rate against the threshold and indicates that as the threshold decreases, more and more pixels are grouped into high-quality, so fewer pixels are needed to do comparison and less time for calculation. From another point of view, if the threshold is larger than or equal to 60%, the error rate is zero. Nevertheless, if the threshold is less than 60%, the error

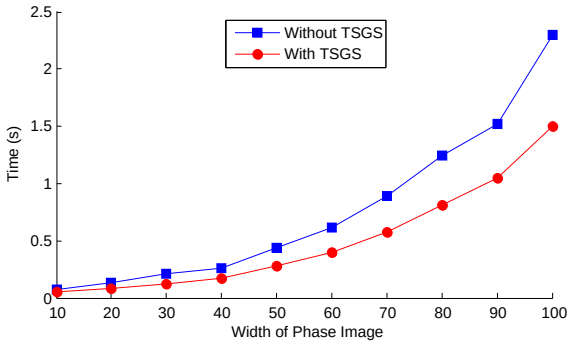

Figure 10. Time comparison between with and without TSGS (I2L2 structure).

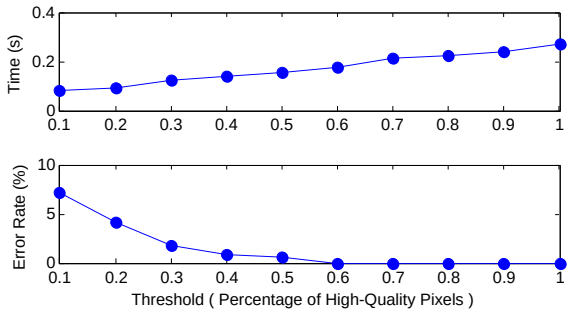

Figure 11. TSGS effect on 41 × 41 logo phase image.

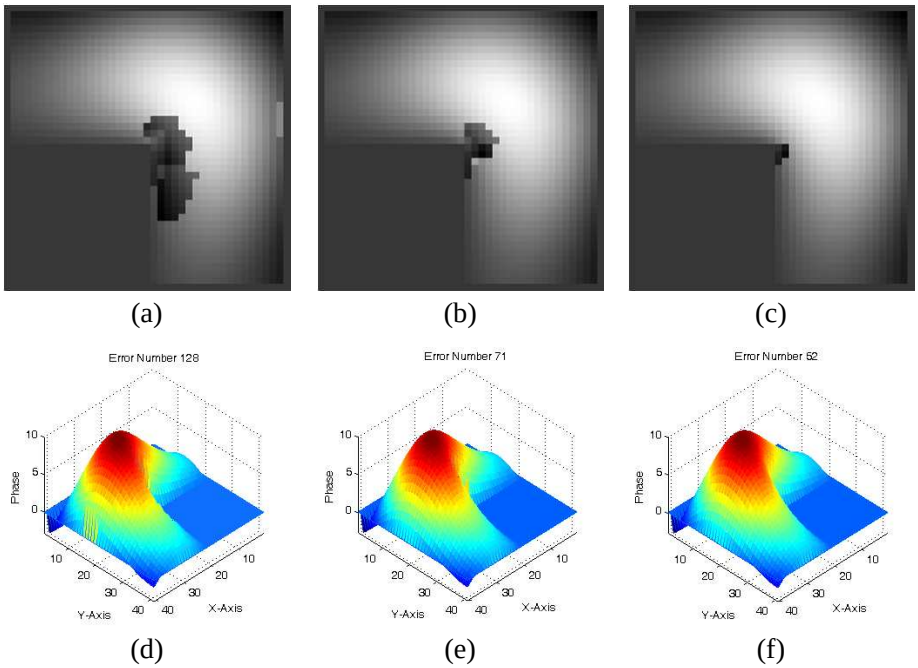

Figure 12. Wrong unwrapping results due to wrong thresholds. (a) Threshold = 0.1. (b) Threshold = 0.2. (c) Threshold = 0.3. (d) 3D rendering of (a). (e) 3D rendering of (b). (f) 3D rendering of (c).

increases as the threshold decreases. For the sake of zero-error and maximal acceleration rate, we chose the threshold as that the high-quality pixels take 60% of all pixels.

The mistaken pixels accumulated in the central area as the threshold was lowering. Figure 12 shows three examples of wrong unwrapping results. The main wrong area is located at the center of the image, which is resulted from the sharp discontinuity at the wrapped image plane seen from Figure 9(b).

4. APPLICATIONS

In this section, we apply our phase unwrapping method to MR images of a healthy volunteer and a monkey. MRI is widely used in hospitals for medical diagnosis [21, 22], staging of disease and for follow-up without exposure to ionizing radiation [23, 24]. Furthermore, we generalize the proposed method to 3D simulation volumetric data.

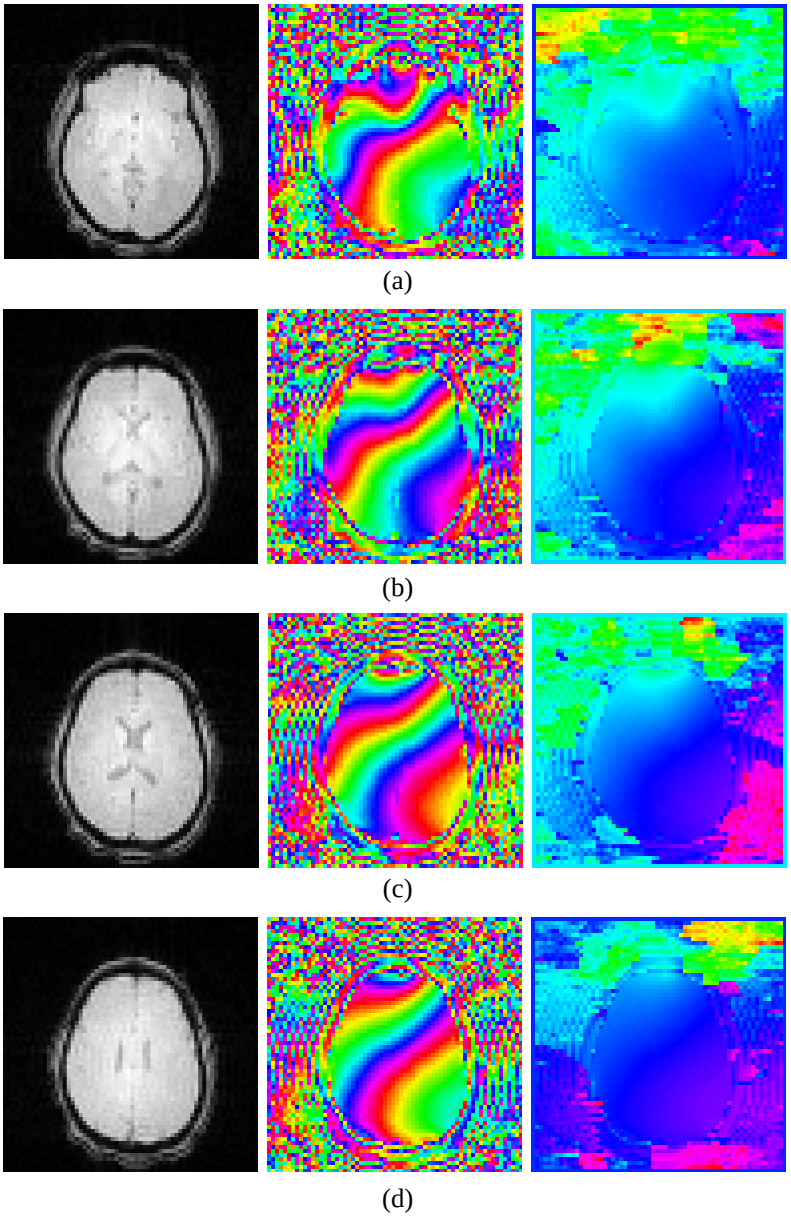

Figure 13. The patient absolute image, wrapped phase, and unwrapped phase of slice. (a) 4. (b) 8. (c) 12. (d) 16.

4.1. Multi-Slice MR images of a Healthy Volunteer

In the first application, we employed our method to a 64-by-64 T2-weighted multi-slice MRIs of human brain and selected four slices (the 4th, 8th, 12th, and 16th) as test images. We use HSV pseudo colormap as image enhancement.

Figure 13 shows the absolute images, wrapped phase images, and unwrapped phase image of the 4th, 8th, 12th, and 16th slices of the brain. It is clear that the phase bears sharp break in the brain area for the wrapped phase. After the unwrapping procedures, the phase is smooth and suitable for the followed processing procedures. The computation times for four slices of the proposed method are 0.44 s, 0.41 s, 0.42 s, and 0.41 s, respectively.

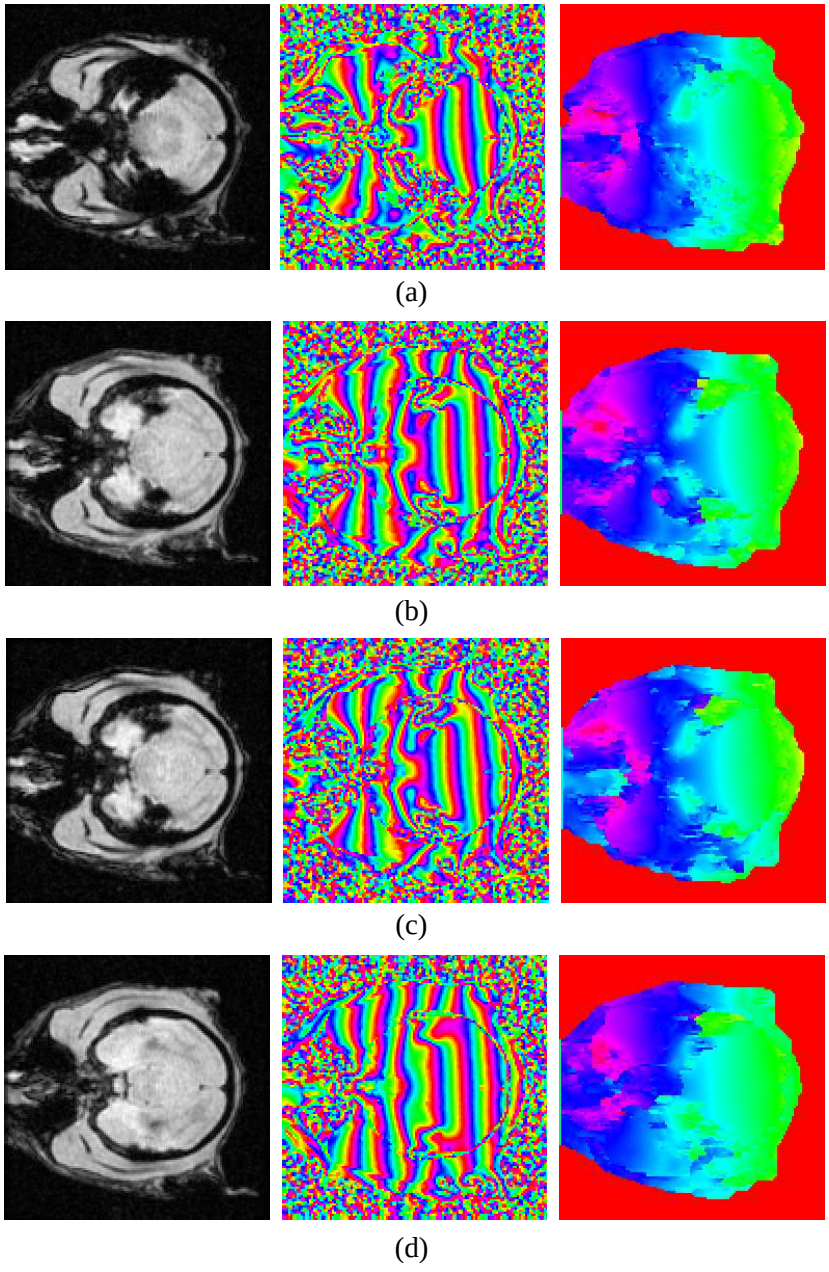

Figure 14. Monkey brain absolute image, wrapped phase, and masked unwrapped phase of slice. (a) 1. (b) 2. (c) 3. (d) 4.

4.2. Multi-Slice MR Images of Monkey

In the second application, we further apply our method to multi-slice brain MR images of a monkey. We generate masks [25] from absolute images to eliminate the influence of background noise on the quality maps.

Figure 14 shows the unwrapped and masked phase image from four slices of the monkey brain image. The phase wrapping in the images of monkey is sharper and more severe than that of human images. In the regions of sinuses and ear channels, signal cancelation was resulted from severe field inhomogeneity caused by the large differences of susceptibilities of air and brain tissues.

This constitutes great challenges for the phase unwrapping because the quality maps are easily contaminated by the noise. As a result, the performances of existing phase unwrapping methods are not satisfactory, including small phase jumps. However, our proposed method performs best and yields smooth unwrapped phases within the brain regions. It is yet a challenging task to repair the phase jump lines, which remains in our future research target. The computation times for the four slices of 256×256 are 18.84 s, 15.81 s, 16.09 s, and 15.83 s.

4.3. 3D Phase Unwrapping Simulation

In the third application, we test our method to 3D phase unwrapping. We demonstrate its capability using simulated a phase data calculated as

$$p = 10 \times x \times (\text{abs}\,(y) + \text{abs}\,(z)) \quad x, y, z \in [0, 1], \quad p \in [0, 20] \tag{5}$$

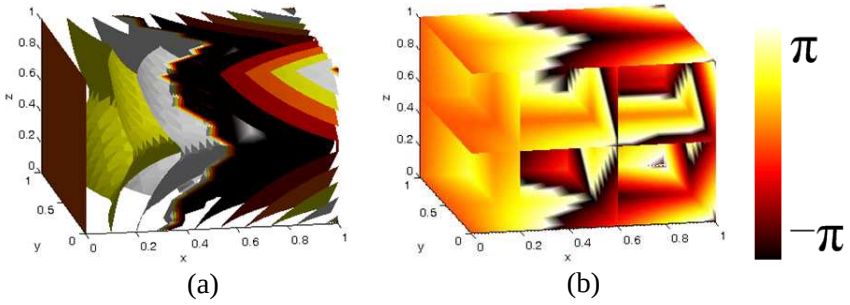

Figure 15. 3D Wrapped phase (the sharp-changing color indicates there are phase jumps. As x increases, the jumps become denser and sharper). (a) Contour plane. (b) Slice plane.

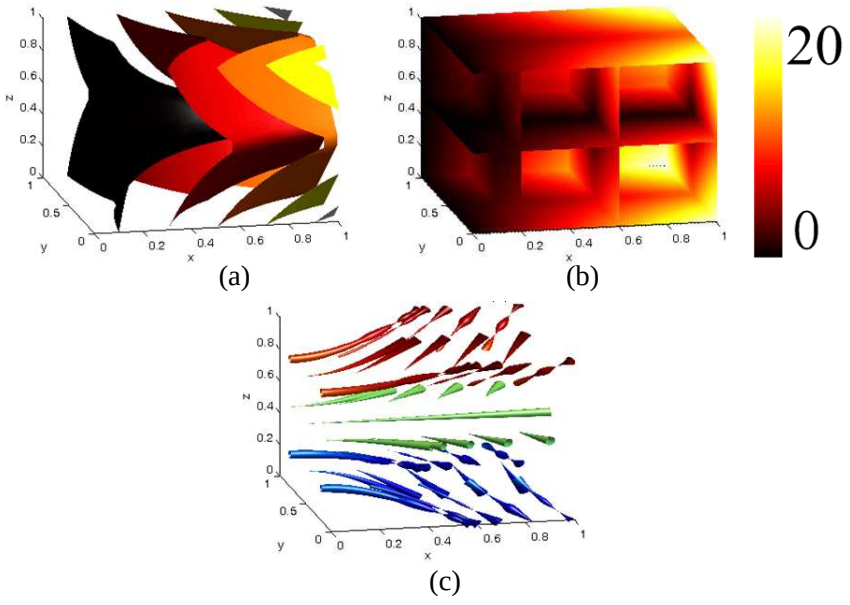

Figure 16. 3D Unwrapped phase. (a) Contour plane. (b) Slice plane. (c) Gradient map.

We do not add noise since the p value covers a large span, leading to a seriously wrapped 3D phase as shown in Figure 15. Because variables x, y, and z are in the range of [0, 1], p is among $[0, 10 * 1 * (1 + 1)] = [0, 20]$. The wrapped phase will fall into the primitive range of $[-\pi, \pi]$.

The wrapped 3D phase images are shown in Figure 15. As in the colored map, the black denotes $-\pi$ and white π. We can see the wrapped from the approximated white and black areas. The sharp-changing color indicates that there are phase jumps. As x increases, the jumps become denser and sharper.

The unwrapping results are shown in Figure 16. The black denotes 0 and the white 20. We see that the phase linearly increases along the x-axis. In the y-z plane, the phase increases gradually outwards, and its contour line is in a diamond shape. The streamline of gradient, namely the direction of the sharpest change in the unwrapped phase, also indicates that the gradient of unwrapped phase continuously expands along the x-axis with no sudden break.

5. CONCLUSION AND FUTURE RESEARCH

In this study, we have discussed a new phase unwrapping method. The highlights of our method lie in three points. 1) We propose an MFPDV as the improved quality map; 2) we introduce in the I2L2 structure; 3) we introduce in the TSGS strategy.

The proposed MFPDV is more robust than PDV, as the mean-filtering procedures suppress noises in the PDV generated quality maps. The unwrapped phase maps based on MFPDV are flatter and less oscillatory than those on PDV (Figure 6). The comparison on an MRI brain image shows that the normalized L_1 norm of MFPDV is only 0.0827, less than that of PDV at 0.0923. Therefore, the MFPDV can be used as a new standard indicator for generating quality map.

I2L2 is an excellent data structure that interweaves the sections of ILL in pre-allocated sequence. The index of the 1D sequence of I2L2 is easily converted to the 2D subordination of the pixel in the image. From our test on ten images of different sizes, the order from best to worst algorithms is I2L2, ILL, LL, and sequence, with regard to computation time (Figure 8). Therefore, the I2L2 structure saves storage memory and operations. It cost about 30% time of QGPU with the sequence structure on average.

TSGS chooses a threshold that divides all pixels as high and low quality groups. A large amount of computation time is avoided due to less comparison times to obtain the high-quality pixels. QGPU with TSGS costs only 65% time of that without TSGS on average.

Our experiment shows the way choosing optimal threshold of TSGS (Figure 11), and wrong thresholds lead to wrong unwrapping results (Figure 12). For the "logo" phase image, setting the threshold T as 60% can guarantee zero-error meanwhile accelerate the algorithm to the most degree. For other phase images, the users need to repeat the procedure and get the corresponding optimal threshold.

The proposed method yields excellent results for multi-slice MR images of human brain (Figure 13) due partly to the high quality of the original images. Contrarily, the performance of the proposed method on monkey images was not as excellent as expected (Figure 14). The unwrapped phase images exhibit disrupted phases in regions of sinuses and ear channels. This is because the original signals were weak and even disappeared in these regions, so the SNRs of the quality map of monkey images were extremely low. Howbeit, our method outperforms conventional QGPU method. The sub-optimal performance of the method in these regions, however, does not have substantial effects on the regions of interest in the brain, where the unwrapped maps show smooth profiles. This example demonstrates the merit and importance of the quality maps in the QGPU method. Figure 16 shows the potential of our method applied to 3D volumetric data.

The future research will focus on the following points. 1) Improving the performance of the proposed method in low signal-to-noise regions of the images; 2) using phase information to segment, classify images [26, 27] more accurately; 3) applying the proposed method to 3D volumetric wrapped data [28].

REFERENCES

1. Zhang, Y., S. Wang, and Z. Dong, "Classification of alzheimer disease based on structural magnetic resonance imaging by kernel support vector machine decision tree," *Progress In Electromagnetics Research*, Vol. 144, 171–184, 2014.
2. Zhang, Y., L. Wu, and G. Wei, "A new classifier for polarimetric SAR images," *Progress In Electromagnetics Research*, Vol. 94, 83–104, 2009.
3. Chin, L., et al., "En face parametric imaging of tissue birefringence using polarization-sensitive optical coherence tomography," *Journal of Biomedical Optics*, Vol. 18, No. 6, 066005, 2013.
4. Ma, S., et al., "Investigation of phase error correction for digital sinusoidal phase-shifting fringe projection profilometry," *Optics and Lasers in Engineering*, Vol. 50, No. 8, 1107–1118, 2012.
5. Huang, H. and Q. Wang, "A method of filtering and unwrapping SAR interferometric phase based on nonlinear phase model," *Progress In Electromagnetics Research*, Vol. 144, 67–78, 2014.
6. Fang, S., et al., "Quality-guided phase unwrapping algorithm based on reliability evaluation," *Appl. Opt.*, Vol. 50, No. 28, 5446–5452, 2011.
7. Egidi, N. and P. Maponi, "A comparative study of two fast phase unwrapping algorithms," *Applied Mathematics and Computation*, Vol. 148, No. 3, 599–629, 2004.
8. Qian, K., S. H. Soon, and A. Asundi, "A simple phase unwrapping approach based on filtering by windowed Fourier transform," *Optics & Laser Technology*, Vol. 37, No. 6, 458–462, 2005.
9. Zhao, M., et al., "Quality-guided phase unwrapping technique: Comparison of quality maps and guiding strategies," *Appl. Opt.*, Vol. 50, No. 33, 6214–6224, 2011.
10. Zhang, S., X. Li, and S. T. Yau, "Multilevel quality-guided phase unwrapping algorithm for real-time three-dimensional shape reconstruction," *Appl. Opt.*, Vol. 46, No. 1, 50–57, 2007.
11. Lu, Y. G. and X. P. Zhang, "Minimum L_0-norm two dimensional phase unwrapping algorithm based on the derivative variance correlation map," *Journal of Physics: Conference Series*, Vol. 48, 308–312, 2006.
12. Zhou, K., M. Zaitsev, and S. Bao, "Reliable two-dimensional phase unwrapping method using region growing and local linear estimation," *Magn. Reson. Med.*, Vol. 62, No. 4, 1085–1090, 2009.
13. Kemao, Q., W. Gao, and H. Wang, "Windowed Fourier-filtered and quality-guided phase-unwrapping algorithm," *Appl. Opt.*, Vol. 47, No. 29, 5420–5428, 2008.
14. Herraez, M. A., et al., "Agglomerative clustering-based approach for two-dimensional phase unwrapping," *Appl. Opt.*, Vol. 44, No. 7, 1129–1140, 2005.
15. Lu, Y., et al., "Weighted-phase-gradient-based quality maps for two-dimensional quality-guided phase unwrapping," *Optics and Lasers in Engineering*, Vol. 50, No. 10, 1397–1404, 2012.
16. Wang, H., et al., "A three-dimensional quality-guided phase unwrapping method for MR elastography," *Phys. Med. Biol.*, Vol. 56, No. 13, 3935–3952, 2011.
17. Liu, S., et al., "Complex-amplitude-based phase unwrapping method for digital holographic microscopy," *Optics and Lasers in Engineering*, Vol. 50, No. 3, 322–327, 2012.
18. Spottiswoode, B. S., et al., "Tracking myocardial motion from cine DENSE images using spatiotemporal phase unwrapping and temporal fitting," *IEEE Trans. Med. Imaging*, Vol. 26, No. 1, 15–30, 2007.
19. Strand, J. and T. Taxt, "Performance evaluation of two-dimensional phase unwrapping algorithms," *Appl. Opt.*, Vol. 38, No. 20, 4333–4344, 1999.
20. Zhang, K., et al., "Phase unwrapping for very large interferometric data sets," *IEEE Transactions on Geoscience and Remote Sensing*, Vol. 49, No. 10, 4048–4061, 2011.
21. Zhang, Y., et al., "A hybrid method for MRI brain image classification," *Expert Systems with Applications*, Vol. 38, No. 8, 10049–10053, 2011.
22. Zhang, Y., et al., "A two-level iterative reconstruction method for compressed sensing MRI," *Journal of Electromagnetic Waves and Applications*, Vol. 25, Nos. 8–9, 1081–1091, 2011.
23. Nordin, L. E., et al., "Cortical responses to amphetamine exposure studied by pCASL MRI and pharmacokinetic/pharmacodynamic dose modeling," *NeuroImage*, Vol. 68, 75–82, 2013.

24. Schaap, K., et al., "Inventory of MRI applications and workers exposed to MRI-related electromagnetic fields in the Netherlands," *European Journal of Radiology*, Vol. 82, No. 12, 2279–2285, 2013.
25. Krüger, D., et al., "Neural correlates of control operations in inverse priming with relevant and irrelevant masks," *NeuroImage*, Vol. 64, 197–208, 2013.
26. Zhang, Y. and L. Wu, "An MR brain images classifier via principal component analysis and kernel support vector machine," *Progress In Electromagnetics Research*, Vol. 130, 369–388, 2012.
27. Zhang, Y., L. Wu, and S. Wang, "Magnetic resonance brain image classification by an improved artificial bee colony algorithm," *Progress In Electromagnetics Research*, Vol. 116, 65–79, 2011.
28. Viotti, M. R., et al., "Processing of noised residual stress phase maps by using a 3D phase unwrapping algorithm," *Optics and Lasers in Engineering*, Vol. 51, No. 7, 890–897, 2013.